Plasmonic-magnetic nanorobots for SARS-CoV-2 RNA detection through electronic readout

Jeonghyo Kim[a], Carmen C. Mayorga-Martinez[a], Jan Vyskočil[a], Daniel Ruzek[b,c], Martin Pumera[a,d,e,*]

[a] Center for Advanced Functional Nanorobots, Department of Inorganic Chemistry, Faculty of Chemical Technology, University of Chemistry and Technology Prague, Technická 5, Prague CZ-166 28, Czech Republic
[b] Laboratory of Emerging Viral Infections, Veterinary Research Institute, Hudcova 70, Brno CZ-621 00, Czech Republic
[c] Institute of Parasitology, Biology Centre of the Czech Academy of Sciences, Branisovska 31, Ceske Budejovice CZ-370 05, Czech Republic
[d] Future Energy and Innovation Laboratory, Central European Institute of Technology, Brno University of Technology, Purkynova 656/123, Brno CZ-616 00, Czech Republic
[e] Department of Medical Research, China Medical University Hospital, China Medical University, No. 91 Hsueh-Shih Road, Taichung, Taiwan

ARTICLE INFO

ABSTRACT

The coronavirus disease 2019 (COVID-19) has prompted an urgent demand for nanotechnological solutions towards the global healthcare crisis, particularly in the field of diagnostics, vaccines, and therapeutics. As an emerging tool for nanoscience and technology, micro/nanorobots have demonstrated advanced performances, such as self-propelling, precise maneuverability, and remote actuation, thus hold great potential to provide breakthroughs in the COVID-19 pandemic. Here we show a plasmonic-magnetic nanorobot-based simple and efficient COVID-19 detection assay through an electronic readout signal. The nanorobots consist of Fe_3O_4 backbone and the outer surface of Ag, that rationally designed to perform magnetic-powered propulsion and navigation, concomitantly the probe nucleic acids transport and release upon the hybridization which can be quantified with the differential pulse voltammetry (DPV) technique. The magnetically actuated nanorobots swarming enables enhanced micromixing and active targeting, thereby promoting binding kinetics. Experimental results verified the enhanced sensing efficiency, with nanomolar detection limit and high selectivity. Further testing with extracted SARS-CoV-2 viral RNA samples validated the clinical applicability of the proposed assay. This strategy is versatile to extend targeting various nucleic acids, thus it could be a promising detection tool for other emerging pathogens, environmental toxins, and forensic analytes.

1. Introduction

Micro/nanorobots are small-scale artificial machines that rationally designed to perform predefined tasks by converting various energies into mechanical motion and various chemical triggers to perform the designed action [1–5]. Along with their advanced performances, such as autonomous self-propelling, precisely maneuverable speed and direction, and remote actuation, these tiny robotic systems have demonstrated great potential for a wide range of applications, including sensing [6–8], targeted delivery [2], microsurgery [9,10], biofilm disruption [11,12], and environmental remediation [13,14]. In particular, micro/nanorobots have been exploited to enhance the analytical performance in biosensing applications [6,7]. The continuous movements of the bioreceptor-functionalized micro/nanorobots lead to microscale fluid mixing and 'on-the-fly' target capturing, which enables the enhanced binding kinetics between biomolecules [2,6]. This strategy offers improved sensitivity and efficiency of the biological target capture and isolation for the proteins [8,15], nucleic acids [16], and cells [17,18].

The coronavirus disease 2019 (COVID-19) pandemic has had a devastating impact on global society, with more than 175 million confirmed cases and 3.7 million deaths over 220 countries (as of June 08, 2021, according to the World Health Organization (WHO) report) [19]. Although the spread of the virus seemed to be mitigated through quick adaptation of communities to the "new normal", such as social distancing, regular sanitization, quarantining [20,21], there are still serious difficulties in epidemic control with the silent transmission of asymptomatic infections [22], and the

emergence and spread of multiple variants [23]. Under these difficulties, continuous diagnostic tests are mandated until the end of the pandemic by achieving herd immunity with an effective vaccine distribution. Fast screening and isolation are the most effective strategy for curbing the disease transmission and are being strongly pursued [24,25]. Current testing largely depends on quantitative reverse transcription polymerase chain reaction (RT-qPCR) assays, which are the most accurate and the gold standard [26]. However, these techniques require laborious procedures and bulky instrumentation, thus it has been pointed out their limitations to be scaled for extensive public health testing [27,28]. Serological lateral-flow assays are supporting as a point-of-care (POC) tool, but also showed suboptimal sensitivity for the early stage of infections [29,30]. In this context, nanotechnology-enabled approaches have an opportunity to provide alternatives for simple and precise viral detection [25,26,31].

Here, we present a simple and efficient COVID-19 detection assay with plasmonic-magnetic nanorobots through an electronic readout platform (see Scheme 1). As a nanoscale building block of nanorobots, the Fe$_3$O$_4$/Au/Ag nanoparticles (NPs) were synthesized by a sequential chemical reduction method. Firstly, under 10 nm Au seeds were formed on the Fe$_3$O$_4$ NPs, which facilitates nucleation and growth of high-density Ag particles, leading to the hierarchically structured Fe$_3$O$_4$/Au/Ag NPs. The nanorobots were readily fabricated by assembling Fe$_3$O$_4$/Au/Ag NPs into rod-shaped microaggregates, which enables controllable propulsion and navigation under the rotating magnetic field. Also, the Ag surface of nanorobots provides the probe DNAs tagging and releasing site depends on hybridization reaction. The magnetic actuation of probe DNA-tagged nanorobots led to promoted target binding reaction with their complementary nucleic acids. The resulting hybridized duplex can be released from the nanorobots due to the change of electrostatic properties. Thus, the quantifying remnant probe DNAs by electrochemical signal confirms the detection of target nucleic acids. Exploiting these versatile concepts, we demonstrated magnetically actuated nanorobot-based detection of the severe acute respiratory syndrome coronavirus 2 (SARS-CoV-2) RNA. Experimental results verified the nanorobot swarming enhanced sensing efficiency, with nanomolar detection limit and high selectivity. Further, the clinical applicability of the proposed assay was validated using extracted SARS-CoV-2 viral RNA samples.

2. Results and discussion

2.1. Plasmonic-magnetic nanorobot-based sensing strategy for SARS-CoV-2 RNA detection

Scheme 1 illustrates the procedure for the plasmonic-magnetic nanorobot-based electrical readout platform for SARS-CoV-2 RNA detection. We first designed the single-stranded DNA (ssDNA) probes with a length of 20 mer, specifically targeting the N gene (nucleocapsid phosphoprotein) sequence of the SARS-CoV-2, which has been recommended for COVID-19 screening tests (Table S1, Supporting Information) [29,32]. The target viral RNA detection exploits different electrostatic properties of the ssDNA probe and its hybridized duplex. Upon incubating with Fe$_3$O$_4$/Au/Ag nanorobots, ssDNA probes can be preferentially attached to the Ag surface of nanorobots via the van der Waals force between nucleobases and metallic nanostructure, as described in previous reports [33–35]. Then, probe DNA-tagged nanorobots are magnetically navigated in the assay solution. Their autonomous movement generates an enhanced mass transfer, and thus higher chance for the target viral RNA capture and hybridization [6,16]. When ssDNA probes are hybridized with complementary target RNAs, the nucleobases are buried within the negatively charged helical phosphate backbones, resulting in electrostatic repulsion is dominant between hybridized

duplex and citrate-coated Fe$_3$O$_4$/Au/Ag nanorobots [36,37]. Therefore, the preloaded ssDNA probes were released by nucleotide hybridization and washed out from the assay solution (Scheme 1a). After completion of the target capturing and releasing step in the assay tubes, the resulting nanorobots were collected and sequentially transferred on the screen-printed electrode (SPE), in which a small neodymium magnet is equipped underneath the working electrode for better locating Fe$_3$O$_4$/Au/Ag nanorobots on the electrode surface. The remnant probe DNAs on the nanorobots can be quantified using direct electrochemical oxidation of the guanine (G) residues by the differential pulse voltammetry (DPV) technique. Consequently, a decrease of the oxidative peak intensity is proportional to the concentration of detected SARS-CoV-2 RNA, which is considered as a positive signal in the assay (Scheme 1b).

2.2. Synthesis and characterization of the plasmonic-magnetic nanoparticles

The Fe$_3$O$_4$/Au/Ag NPs, as a building block for assembling nanorobots, were synthesized through a facile two-step sequential chemical reduction method (Fig. S1, Supporting Information). Firstly, Au(III) precursor is reduced by a strong reducing agent (NaBH$_4$) in the presence of Fe$_3$O$_4$ NPs, leading to the formation of <10 nm Au seeds on the surface of the magnetic core (Fig. 1a) [38,39]. Then further reacted with silver enhancer solution, in which the gold surface provides nucleation site and accelerates Ag growth on it, resulting in high-density of Ag particles are readily assembled on the Au seeded-Fe$_3$O$_4$ NPs (Fig. 1b, see details in Section 4) [40]. The selected area electron diffraction (SAED) pattern shows a superposition of Fe$_3$O$_4$, Au, and Ag lattices, showing five distinguishable planes of (111), (200), (220), (311), (222) from Ag and three distinguishable (−102), (−104), and (141) plane from iron oxides. Other planes overlap with the Au/Ag planes (Fig. 1c). Transmission electron microscopy (TEM) and energy-dispersive X-ray spectroscopy (EDS) analysis shown in Fig. 1d and f confirm that Fe, O, Au, and Ag elements are hierarchically distributed over the hybrid structures. The average size of the Ag, estimated from 50 particles, was ~156 nm that is comparable to the Fe$_3$O$_4$ core (Fig. 1e). Further high-angle annular dark-field scanning transmission electron microscopy (HAADF-STEM) images and morphological analysis for the sequential fabrication of the Fe$_3$O$_4$/Au/Ag NPs are shown in Fig. S2, Supporting Information.

2.3. Magnetic actuation of the plasmonic-magnetic nanorobots

In our approach, the nanorobots were constructed by assembling Fe$_3$O$_4$/Au/Ag NPs into rod-shaped microaggregates upon the application of a transversal rotating magnetic field. The assembly process is governed by a balance of magnetic dipole-dipole interaction and electrostatic repulsion from charged NPs, thereby their size limited in length of 2.49 ± 0.59 μm, and width of 1.10 ± 0.28 μm as shown in Fig. S3, Supporting Information. This structure makes them sufficient magnetization to generate the desired movement [9,41,42]. Magnetic propulsion and navigation are controlled by a transversal rotating magnetic field, as described in the previous report [9]. A rotating magnetic field applied in a vertical (x-z) plane exerts perpendicular magnetic torque (τ_m) on the Fe$_3$O$_4$/Au/Ag nanorobots, thus they rotate along their long axis in the same x-z plane synchronized with a frequency (f) of an external magnetic field. In this configuration, the drag force closed to the boundary is stronger than the other side, which makes a velocity difference at both ends of the nanorobots, allowing propulsion with a tumbling motion parallel to the horizontal (x-y) plane [9,41,42].

The prolusion velocity can be tuned by adjusting the transversal rotating magnetic field frequency. As shown in Fig. 2a and
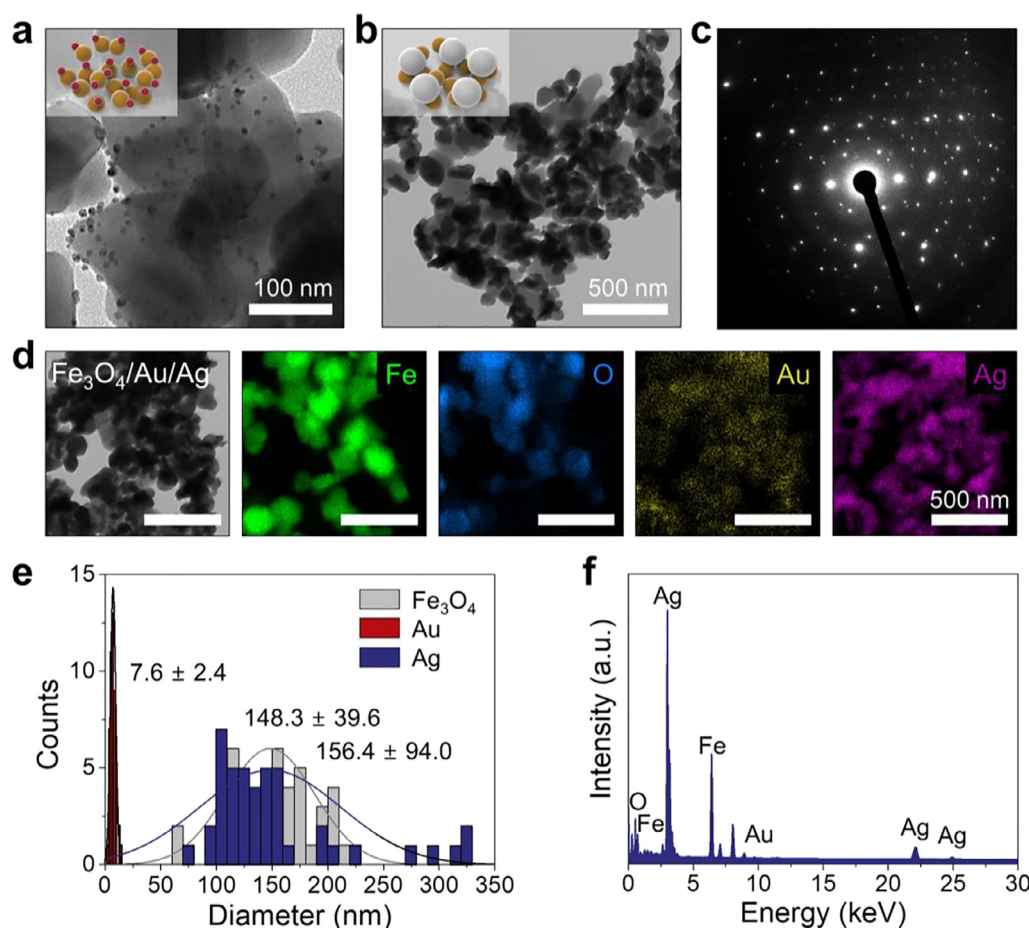
Fig. 1. Characterization of Fe$_3$O$_4$/Au/Ag nanoparticles. (a,b) TEM images of Au seeded-Fe$_3$O$_4$ particles (a) and after Ag enhancement (b). (c) SAED pattern, and (d) TEM-EDS mapping of Fe$_3$O$_4$/Au/Ag NPs. (e) Size distributions of Fe$_3$O$_4$, Au, and Ag, as measured by 50 particles from TEM images. (f) EDS spectrum from (d).

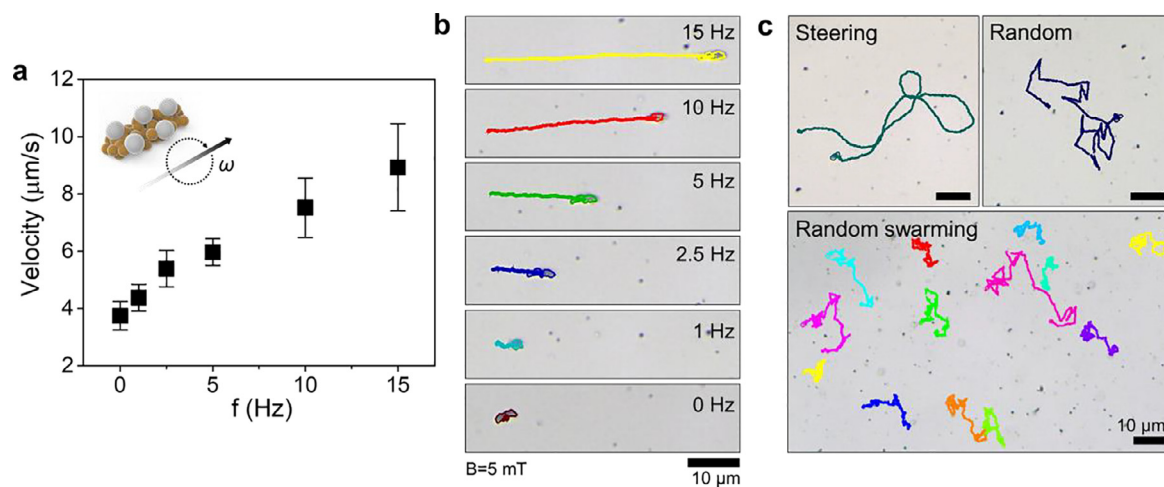**Fig. 2.** Magnetic propulsion and navigation of the Fe$_3$O$_4$/Au/Ag nanorobots. (a, b) Average velocity (a) and representative swimming trajectories (b) of the Fe$_3$O$_4$/Au/Ag nanorobots at a different frequency (Hz) of magnetic field ($n = 15$, error bars represent the standard deviation of the mean). (c) Manual and programmable navigation of the Fe$_3$O$_4$/Au/Ag nanorobots.

b, the average velocity of Fe$_3$O$_4$/Au/Ag nanorobots increases linearly with the actuation frequency and then reached a maximum speed of 8.9 μm s^{-1} ($\approx$3.6 body length s^{-1}) at the frequency of 15 Hz and magnetic field strength of 5 mT. Beyond this step-out frequency (15 Hz), the nanorobots start to lost synchronous rotation and straight movement, which is consistent with previous reports [9,41]. Their real-time propulsion in various frequencies is compared in Supplementary Movie 1. Furthermore, the propulsion direction can be steered by controlling the angle of the rotation plane on a two-dimensional surface. In this study, we demonstrated two different navigation modes, i.e., manually steering and automated random directional propulsion: (i) In the steering mode, the rotational plane angle can be manipulated manually, thus the nanorobots can be propelled and steered on the x-y plane in a
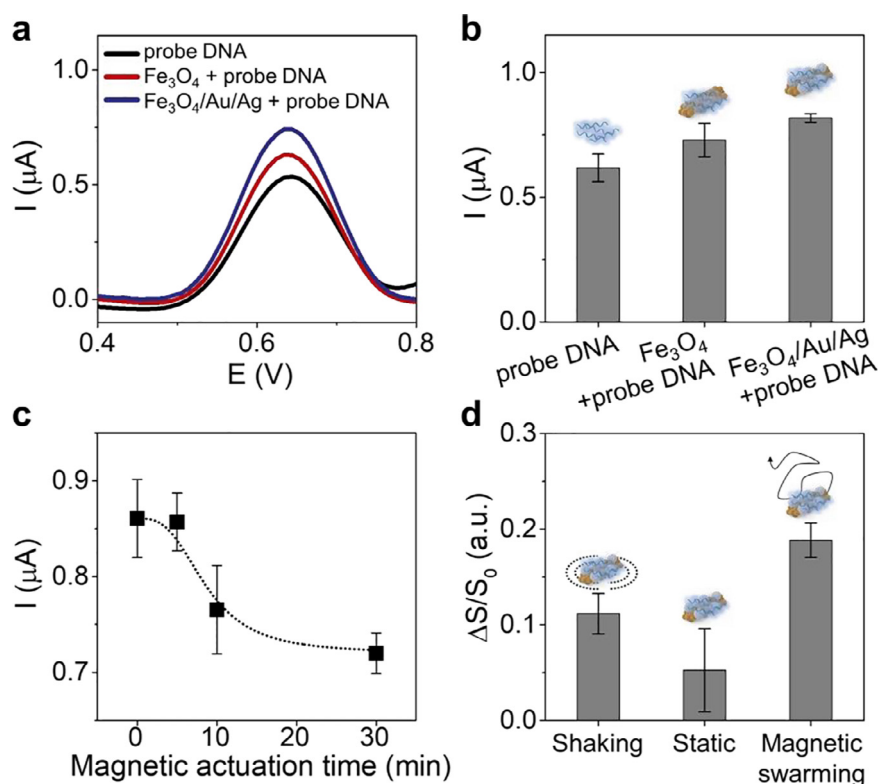
Fig. 3. Optimization and efficiency of the nanorobot-based assay. (a,b) DPV measurements for electro-oxidation of the guanine residues with and without $Fe_3O_4/Au/Ag$ NPs. Representative DPVs (a) and average intensity of DPV peaks (b). (c) Optimization target RNA detection depends on the magnetic actuation time. (d) Comparison of static-, shaking-, and magnetic swarming based assay for the SARS-CoV-2 RNA sensing. Data are presented as mean ± s.d. of triplicate measurements.

controllable fashion. (ii) In the automated propulsion mode, we programmed a magnetic controller that can generate random directional rotation angle in every second, and thus the nanorobot can perform a continuous movement with random angular change. The trajectory of nanorobot was predefined by a pseudo-random sequence with a uniform distribution of angles (α_i, $0 \le \alpha_i < 360°$, $i = 1, 2, … N$), and delay time (d, sec) between angle changes as shown in Fig. S4, Supporting Information. In both modes, the nanorobots instantaneously respond to the rotational plane angle change, because of the negligible inertial force,[1,3] therefore the precise directional maneuvering was possible as shown in Fig. 2c and Supplementary Movie 2. Consequently, we exploited the automated random mode propulsion for further autonomous target capturing and releasing in assay solution, in which the group of nanorobots showed a continuous random directional movement in forward and backward (Supplementary Movie 3). This random mode swarming allows quick micro-fluid mixing and enhanced binding reaction in the entire sample solution.

2.4. Efficiency, sensitivity, and selectivity of SARS-CoV-2 RNA detection

Using programmed random mode swarming of $Fe_3O_4/Au/Ag$ nanorobots and hybridization-based ssDNA probe detachment mechanism, we demonstrated the nanorobot-based electrical readout platform for simple and efficient SARS-CoV-2 RNA detection. In the proposed assay, specific targeting of SARS-CoV-2 RNA was transduced to the depletion of probe DNAs on the nanorobot body, which can be quantified by measuring the electrochemical oxidation peak of guanine (G) residues using differential pulse voltammetry (DPV) technique. To validate the role of $Fe_3O_4/Au/Ag$ in the electrochemical analysis, we evaluated the electrooxidation of ssDNA probes with and without NPs (Fig. 3a and b). The DPV mea-

surement for 2 μM of ssDNA probes on the SPEs shows a clear oxidative peak at 0.63 V, relying on the irreversible oxidation of G to 8-oxoguanine [43]. In addition, the current intensity of the G oxidation peak was enhanced 1.2-, and 1.4-times when the same concentration of probe DNAs (2 μM) was incubated with Fe_3O_4 and $Fe_3O_4/Au/Ag$ NPs, respectively. This observation could be attributed to that the NPs can provide a large surface area for effectively adsorbing ssDNA probes on the electrode surface, and the high electrical conductivity of Ag particles can enhance the electrooxidation of guanine residues [44–46]. Conversely, in the case of only $Fe_3O_4/Au/Ag$ NPs deposited without ssDNA probes, no peaks were observed during the potential scanning (Fig. S5, Supporting Information).

Next, we evaluated the kinetics of the assay depending on the magnetic actuation time to yield the highest sensing performance. The oxidative G peak currents were measured while varying the reaction time under the rotating magnetic field, confirming that the 30 min magnetic actuation produced a maximum decrease of DPV signal, then saturated (Fig. 3c). Therefore, 30 min magnetic actuation was chosen as the optimum time for further assays. Subsequently, the efficiency of magnetic swarming on the target RNA sensing is compared with static- and shaking-based assays (Fig. 3d). We defined the analytical signal as S_0-S_S/S_0, i.e., $\Delta S/S_0$, where S_S and S_0 denote the surface areas of G oxidation curve with and without target RNA, respectively. In this way, the sensing signal can be expressed directly proportional to the concentration of the target RNA that provides an easy to interpret quantitative readout for the presence of the target RNA. In comparison to the vortex shaking of assay tube at 800 rpm, the magnetic swarming-based assay at 15 Hz generates a 1.7-fold higher signal, that confirms the enhanced micromixing and mass transfer by magnetically actuated nanorobots are effective for improved RNA capture and hybridization.
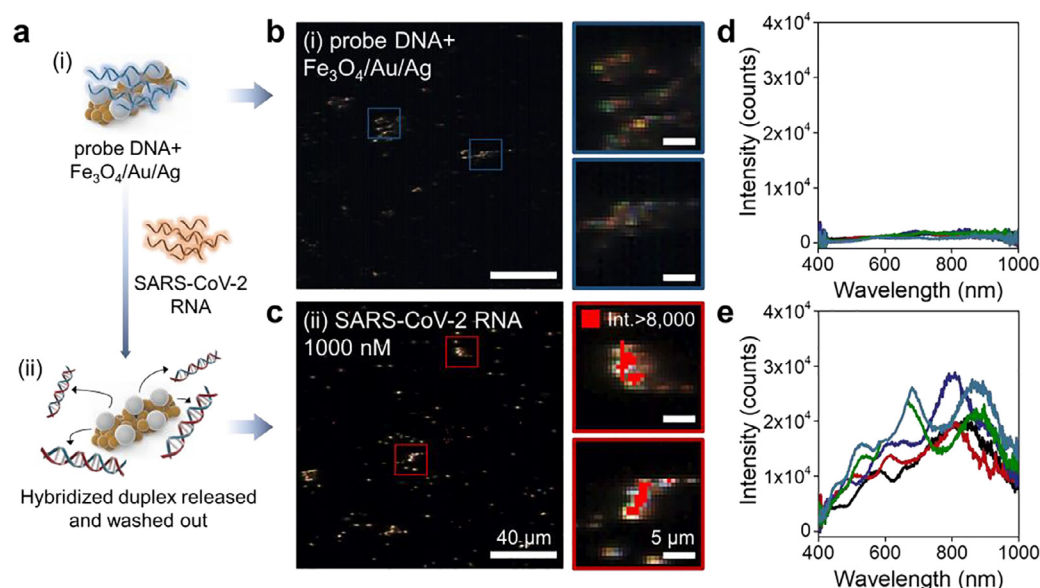
Fig. 4. Hyperspectral dark-field microscopy (HDFM) analysis of the Fe$_3$O$_4$/Au/Ag nanorobots before and after target RNA detection. (a) Schematic of HDFM analysis samples: (i) probe DNA attached nanorobots, and (ii) after reacted with 1000 nM of SARS-CoV-2 RNA. (b,c) Hyperspectral microscope images of the sample (i), and (ii) in (a). Red overlaid spots indicate pixels having peak intensity over 8000. (d,e) Spectra collected from 5 pixels shown in the magnified images in b and c.

To further confirm the sensing strategy that is based on the tunable affinity of the probe DNAs to the nanorobots, hyperspectral dark-field microscopy (HDFM) analysis was carried out. Fig. 4 shows the HDFM images and scattering spectra of the probe DNA-tagged nanorobots before and after assayed with 1000 nM of SARS-CoV-2 RNA under the standard condition (see details in Section 4). In their initial state, nanorobots were fully covered with ssDNA probes, which strongly shields the scattering of Ag particles. This effect can be observed under a dark-field image as dimmed objects and reduced scattering intensities (Fig. 4a(i), b, and d). In contrast, after hybridization and washing out the released hybridized duplexes, the scattering of Ag is recovered, and shiny particles are appeared (Fig. 4a(ii) and c). Using a particle filter algorithm, the localization of pixels with a peak intensity of over 8000 counts was mapped in hyperspectral images. As shown in magnified images in Fig. 4c, red overlaid pixels spread over the nanorobots. Moreover, spectrum profiles of 5 pixels among them show strong scattering peaks in multiple wavelengths (Fig. 4e). The significant increase in the spectral peaks after the hybridization of ssDNA probes supported the successful sensing mechanism used in the assay.

Following the assay optimization and efficiency test, we evaluated the analytical performance of the nanorobot-based electronic readout platform for the SARS-CoV-2 RNA detection. A standard curve was characterized using serially diluted target SARS-CoV-2 RNA. It showed a logarithmic linear relationship in the range of 5–1000 nM with a regression equation of $y = 0.024 \ln(x) + 0.007$ ($R^2 = 0.967$), where y is $\Delta S/S_0$ and x is the concentration of target RNA strain (Fig. 5a and b). The limit of detection (LOD), defined as the concentration corresponding to a signal that is equal to three times the standard deviation of the blank, was calculated to be 1.8 nM. A selectivity test was performed using equal concentrations (1000 nM) of complementary (SARS-CoV-2 RNA), single-base-mismatch, and non-complementary sequences (Fig. 5c and Table S1, Supporting Information). Single base mismatched strains showed an obvious signal decrease compared with perfectly matched sequences, due to the reduced efficiency of hybridization. Non-complementary sequences are not detected in the assay, because they are not reacted with ssDNA probes and left unhybridized form. Finally, to validate the potential for practical clinical use, we tested the viral RNA samples extracted from the SARS-CoV-2 virus. The sensing signal showed linear responses to a series of SARS-CoV-2 RNA in the range of 1.4 ng/mL to 1.4 mg/mL ($y = 0.041 \ln(x) - 0.035$, $R^2 = 0.951$), and the LOD was 6.1 ng/mL (see Fig. 5d). These quantitative analysis results verified that the nanorobot-based assay can be applied for actual clinical sample testing.

3. Conclusion

In summary, we have demonstrated simple and efficient plasmonic-magnetic nanorobot-based SARS-CoV-2 RNA detection assay. The nanorobots consist of Fe$_3$O$_4$ backbone and the outer surface of Au and Ag, that fabricated by a facile colloidal assembly process. Along the transversal rotating magnetic field, the Fe$_3$O$_4$/Au/Ag NPs pulled together and form rod-shaped microassemblies, thereby achieving sufficient magnetization for further magnetic actuation. The resulting Fe$_3$O$_4$/Au/Ag nanorobots actively moved with a tumbling motion under the transversal rotating magnetic field, showing precisely maneuverable speed and directionality. We demonstrated manually steered-, and programmed random directional propulsion at the maximum speed of 8.9 μm s^{-1} ($\approx$3.6 body length s^{-1}). The Ag metal surface aided the probe DNAs transport and release upon the hybridization, which is microscopically evidenced by hyperspectral dark-field imaging analysis. Particularly, the automated random swarming mode was exploited to facilitate fluid mixing and molecular binding kinetics, leading to a 1.7-fold higher sensing signal compared to the typical vortex shaking method. The proposed method showed a nanomolar detection limit without including an electro-catalytic or enzymatic amplification mechanism, and which is similar or higher sensitivity compared with recently reported SPE-based nucleic acid assays (Table S2, Supporting Information). Thus, the detection sensitivity could possibly be further increased upon the combination with electrode modification or nucleic acid amplification (i.e., PCR) technique. In addition, the high selectivity of the assay was evaluated with single-base-mismatch, and non-complementary sequences. Further testing with extracted SARS-CoV-2 RNA samples validated the clinical applicability of the proposed assay. This strategy is versatile to extend targeting various nucleic acids, thus it
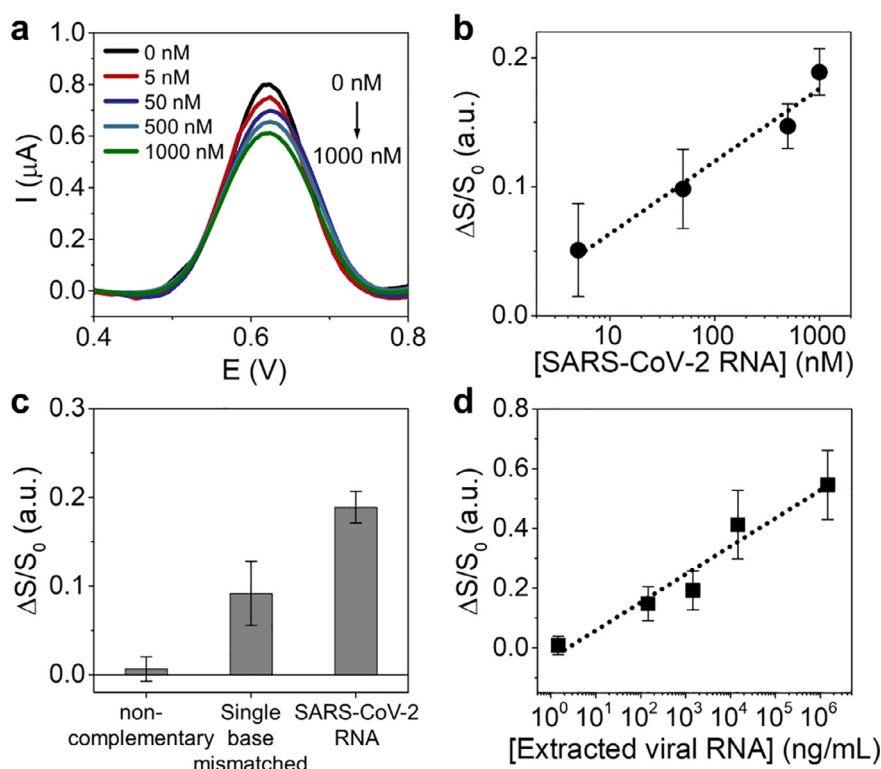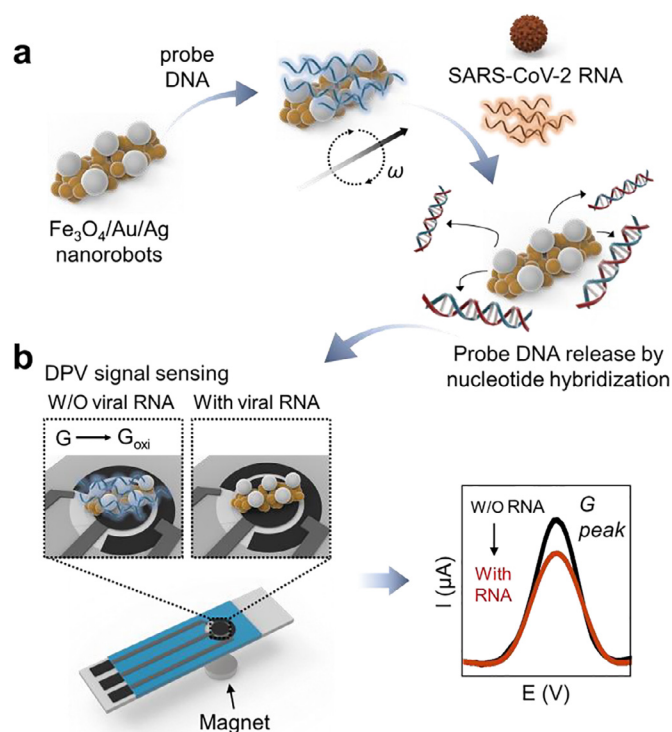
Fig. 5. SARS-CoV-2 RNA detection with swarming Fe_3O_4/Au/Ag nanorobots and electrical readout platform. (a,b) Representative DPVs (a) and calibration curve (b) of the assay with different amounts of target SARS-CoV-2 RNA strain. (c) Selectivity evaluation against different non-target strains. (d) Detection linearity of the extracted SARS-CoV-2 RNA samples. Data are presented as mean ± s.d. of triplicate measurements.

Scheme 1. Schematics of plasmonic-magnetic nanorobots-based electrical readout platform for SARS-CoV-2 RNA detection. (a) Proposed sensing strategy: collective swarming of probe DNA-tagged Fe_3O_4/Au/Ag nanorobots captures target RNA and releases hybridized duplex. (b) Electrical readout of guanine oxidation with DPV signal on the screen-printed electrode.

could be a promising detection tool for other emerging infectious diseases, environmental toxins, and forensic analytes.

4. Experimental section

4.1. Materials

Iron (II, III) oxide nanopowder (product No. 637106), gold(III) chloride trihydrate ($HAuCl_4 \cdot 3H_2O$), silver nitrate ($AgNO_3$), trisodium citrate (TSC) dehydrate ($C_6H_5Na_3O_7 \cdot 2H_2O$), sodium borohydride ($NaBH_4$), hydroquinone ($C_6H_6O_2$), citric acid ($C_6H_8O_7$), sodium chloride (NaCl), phosphate buffer solution (PBS, 1 M, pH 7.4) were obtained from Sigma−Aldrich Inc. (St. Louis, MO). All aqueous solutions were prepared using Milli-Q-grade (>18.2 mΩ/cm) deionized (DI) water. All synthetic oligonucleotides were purchased from Sigma-Aldrich (Darmstadt, Germany), and the sequences are shown in Table S1, Supporting Information. The viral RNA was isolated from SARS-CoV-2 virus (strain SARS-CoV-2/human/Czech Republic/951/2020, isolated from a clinical sample at the National Institute of Public Health, Prague) using QIAmp Viral RNA mini kit (Qiagen), according to the manufacturer's recommendations. The virus was passaged in Vero E6 cells five times before its use in this study.

4.2. Synthesis of Fe_3O_4/Au/Ag nanoparticles

The Fe_3O_4/Au/Ag NPs were synthesized by the two-step sequential chemical reduction method. The commercially available Fe_3O_4 nanopowder (ca. 150 nm in diameter, product No. 637106, Sigma−Aldrich) was used as a magnetic core. To prepare Au seed-coated magnetic cores, 4 mg of Fe_3O_4 NPs were dissolved in 2 mL of DI water, followed by mixing with 2.5 mM $HAuCl_4$ (2 mL) and 5 mM TSC (2 mL). Then, 100 μL of freshly prepared 0.1 M

NaBH$_4$ was added to the mixture solution while irradiating ultrasound [38,39]. The solution turned dark reddish immediately after adding NaBH$_4$, indicating Au seeds formation. The ultrasound irradiation continued for 30 min, followed by washing with DI water three times. Ag particles are grown on the Au seeds, using a silver enhancement process according to the previous report [40]. Briefly, a hydroquinone-citrate buffer solution (pH 3.6) was prepared by dissolving 0.1 M citric acid, 0.1 M trisodium citrate, and 0.1 M hydroquinone. The silver enhancer solution was prepared by mixing 4.25 mL of hydroquinone-citrate buffer with 0.75 mL of 0.1 M AgNO$_3$ solution. Next, the as-prepared Au seeded Fe$_3$O$_4$ NPs (1 mg/mL) were mixed with the silver enhancer solution as a volume ratio of 1:1, then agitated at 600 rpm, for 20 min under low light. The resulting particles were then washed with DI water three times and used for nanorobot assembly.

4.3. Assembly of nanorobots and magnetic actuation

The magnetic actuation of nanorobots was performed using a transversal rotating magnetic field generated by a home-made tri-axial coil setup. More details about the magnetic manipulation system can be found in the authors' previous report [9]. Briefly, the system consists of three pairs of electromagnetic coils that were mounted on an inverted optical microscope (Olympus CKX53, equipped with a Basler acA-1920-155um monochrome CMOScamera) and is capable of generating the transversal rotating magnetic field with a controllable intensity and frequency by the connected power supply. For the preparation of nanorobots, the designated low concentration (<0.1 mg/mL) of the Fe$_3$O$_4$/Au/Ag NPs were prepared in an aqueous solution, and applied the transversal rotating magnetic field, at 5 mT, 15 Hz, for 1 min. During the magnetic field application, NPs gradually closed each other and formed rod-shaped micro-assemblies (Fig. S3, Supporting Information). Over this designated concentration, the assembly process led to uncontrollable aggregation, thus occurred sedimentation of long chain-like structures. The motion was recorded at a 50 X objective lens. NIS-Elements AR 3.2 software was used to obtain the tracking trajectories and average speed from the recorded videos. In typical motion analysis, 10 μL of nanorobot solution was dropped on a glass slide and located inside the electromagnetic coils. The rotational frequency of the magnetic field, and the steering plane angle are independently controlled by the power supply of the magnetic coil device.

4.4. Magnetically actuated nanorobot-based target RNA sensing

In the typical assay, the Fe$_3$O$_4$/Au/Ag nanorobots (0.1 mg/mL, 1 mL) were washed with 0.1 M PBS buffer (pH 7.4) and incubated with 2 μM of DNA probes (10 μL) at 800 rpm, 42°C, for 1 h. The resultant solution washed three times with sequential buffer solutions, TSC buffer 1 (0.75 M NaCl + 75 mM trisodium citrate, pH 7.0), TSC buffer 2 (0.30 M NaCl + 30 mM trisodium citrate, pH 7.0), and 0.1 M PBS buffer. Then, redispersed in 0.1 M PBS buffer with 0.2 mg/mL concentration. Finally, 50 μL of the probe DNA-attached nanorobots were incubated with target RNA samples (10 μL). This step was performed inside the electromagnetic coil setup, with applied the random mode rotating magnetic field at 5 mT, 15 Hz, for 30 min. The assayed solution was washed with 0.1 M PBS buffer three times, then redispersed in the same buffer. After completion of the target sensing step, the working electrode of SPE was modified by drop-casting 5 μL of the assayed sample, in which a small neodymium magnet is equipped underneath the electrode for better locating magnetic nanomaterials. The DPV measurement was conducted in 0.1 M PBS buffer solution (pH 7.4) with operating parameters of 50 ms modulation time, 0.5 s interval time, 10 mV step potential, 50 mV modulation amplitude, and 20 mV s^{-1} scan rate.

Unless otherwise stated, all assays were carried out with this standard condition.

4.5. Characterization

The morphologies of the Fe$_3$O$_4$/Au/Ag NPs were characterized by scanning electron microscopy (MAIA3, Tescan, Czech Republic) equipped with an energy dispersive X-ray detector (Oxford Instruments, UK), and transmission electron microscopy (Jeol JEM-2200FS, Japan). The dark-field microscopic imaging and hyperspectral data were obtained by the CytoViva Hyperspectral Imaging System (CytoViva Inc., USA). For the electrochemical analysis, disposable screen-printed electrodes (eDAQ Instruments, Europe) with a three-electrode configuration were used. The differential pulse voltammetry (DPV) measurement was performed using Autolab PGSTAT204 workstation (Metrohm, Netherlands) that operated by a NOVA 2.1 software. The raw data were processed with a baseline correction of guanine oxidative peak using a NOVA 2.1 software.

Declaration of Competing Interest

There are no conflicts to declare.

CRediT authorship contribution statement

Jeonghyo Kim: Conceptualization, Project administration, Investigation, Visualization, Formal analysis, Validation, Writing – original draft, Writing – review & editing. **Carmen C. Mayorga-Martinez:** Conceptualization, Investigation, Formal analysis, Writing – review & editing. **Jan Vyskočil:** Methodology, Investigation, Writing – review & editing. **Daniel Ruzek:** Validation, Writing – review & editing. **Martin Pumera:** Supervision, Conceptualization, Resources, Writing – review & editing.

Acknowledgments

Supplementary materials

Supplementary material associated with this article can be found, in the online version, at doi:10.1016/j.apmt.2022.101402.

References

[1] H. Zhou, C.C. Mayorga-Martinez, S. Pané, L. Zhang, M. Pumera, Magnetically driven micro and nanorobots, Chem. Rev. 121 (2021) 4999–5041, doi:10.1021/acs.chemrev.0c01234.

[2] J. Li, B.E.F. de Ávila, W. Gao, L. Zhang, J. Wang, Micro/nanorobots for biomedicine: delivery, surgery, sensing, and detoxification, Sci. Robot. 2 (2017) eaam6431, doi:10.1126/scirobotics.aam6431.

[3] S. Palagi, P. Fischer, Bioinspired microrobots, Nat. Rev. Mater. 3 (2018) 113–124, doi:10.1038/s41578-018-0016-9.

[4] B. Wang, K. Kostarelos, B.J. Nelson, L. Zhang, Trends in micro-/nanorobotics: materials development, actuation, localization, and system integration for biomedical applications, Adv. Mater. (2020) 2002047, doi:10.1002/adma.202002047.

[5] C.K. Schmidt, M. Medina-Sánchez, R.J. Edmondson, O.G. Schmidt, Engineering microrobots for targeted cancer therapies from a medical perspective, Nat. Commun. 11 (1) (2020) 5618, doi:10.1038/s41467-020-19322-7.

[6] J. Wang, Self-propelled affinity biosensors: moving the receptor around the sample, Biosens. Bioelectron. 76 (2016) 234–242, doi:10.1016/j.bios.2015.04.095.

[7] J.Guan Kong, M. Pumera, Micro- and nanorobots based sensing and biosensing, Curr. Opin. Electrochem. 10 (2018) 174–182, doi:10.1016/j.coelec.2018.06.004.

[8] C.C. Mayorga-Martinez, M. Pumera, Self-propelled tags for protein detection, Adv. Funct. Mater. 30 (2020) 1906449, doi:10.1002/adfm.201906449.

[9] J. Vyskocil, C.C. Mayorga-Martinez, E. Jablonska, F. Novotny, T. Ruml, M. Pumera, Cancer cells microsurgery via asymmetric bent surface Au/Ag/Ni microrobotic scalpels through a transversal rotating magnetic field, ACS Nano 14 (2020) 8247–8256, doi:10.1021/acsnano.0c01705.

[10] F. Soto, J. Wang, R. Ahmed, U. Demirci, Medical micro/nanorobots in precision medicine, Adv. Sci. 7 (2020) 2002203, doi:10.1002/advs.202002203.

[11] K. Villa, J. Viktorova, J. Plutnar, T. Ruml, L. Hoang, M. Pumera, Chemical microrobots as self-propelled microbrushes against dental biofilm, Cell Rep. Phys. Sci. 1 (9) (2020) 100181, doi:10.1016/j.xcrp.2020.100181.

[12] M. Ussia, M. Urso, K. Dolezelikova, H. Michalkova, V. Adam, M. Pumera, Active light-powered antibiofilm ZnO micromotors with chemically programmable properties, Adv. Funct. Mater. (2021) 2101178, doi:10.1002/adfm.202101178.

[13] L. Dekanovsky, B. Khezri, Z. Rottnerova, F. Novotny, J. Plutnar, M. Pumera, Chemically programmable micromotorss weaving a web from hormones, Nat. Mach. Intell. 2 (11) (2020) 711–718, doi:10.1038/s42256-020-00248-0.

[14] Y. Ying, A.M. Pourrahimi, Z.k. Sofer, S. Matějková, M. Pumera, Radioactive uranium preconcentration via self-propelled autonomous microrobots based on metal–organic frameworks, ACS Nano 13 (2019) 11477–11487, doi:10.1021/acsnano.9b04960.

[15] E. Morales-Narváez, M. Guix, M. Medina-Sánchez, C.C. Mayorga-Martinez, A. Merkoçi, Micromotor enhanced microarray technology for protein detection, Small 10 (2014) 2542–2548, doi:10.1002/smll.201303068.

[16] D. Kagan, S. Campuzano, S. Balasubramanian, F. Kuralay, G.U. Flechsig, J. Wang, Functionalized micromachines for selective and rapid isolation of nucleic acid targets from complex samples, Nano Lett. 11 (2011) 2083–2087, doi:10.1021/nl2005687.

[17] M. Medina-Sánchez, L. Schwarz, A.K. Meyer, F. Hebenstreit, O.G. Schmidt, Cellular cargo delivery: toward assisted fertilization by sperm-carrying micromotors, Nano Lett. 16 (2016) 555–561, doi:10.1021/acs.nanolett.5b04221.

[18] H. Wang, M. Pumera, Micro/nanomachines and living biosystems: from simple interactions to microcyborgs, Adv. Funct. Mater. 28 (2018) 1705421, doi:10.1002/adfm.201705421.

[19] World Health Organization, COVID-19 weekly epidemiological update, edition 43, 8 June 2021, https://www.who.int/publications/m/item/weekly-epidemiological-update-on-covid-19---8-june-2021 (accessed: June 26, 2021).

[20] K.P.A. Kumar, M. Pumera, 3D-Printing to mitigate COVID-19 pandemic, Adv. Funct. Mater. 31 (2021) 2100450, doi:10.1002/adfm.202100450.

[21] O.J. Wouters, K.C. Shadlen, M. Salcher-Konrad, A.J. Pollard, H.J. Larson, Y. Teerawattananon, M. Jit, et al., Challenges in ensuring global access to COVID-19 vaccines: production, affordability, allocation, and deployment, The Lancet 397 (2021) 1023–1034, doi:10.1016/S0140-6736(21)00306-8.

[22] Q.X. Long, X.J. Tang, Q.L. Shi, Q. Li, H.J. Deng, J. Yuan, J.L. Hu, W. Xu, Y. Zhang, F.J. Lv, Clinical and immunological assessment of asymptomatic SARS-CoV-2 infections, Nat. Med. 26 (2020) 1200–1204, doi:10.1038/s41591-020-0965-6.

[23] A. Fontanet, B. Autran, B. Lina, M.P. Kieny, S.S.A. Karim, D. Sridhar, SARS-CoV-2 variants and ending the COVID-19 pandemic, The Lancet 397 (2021) 952–954, doi:10.1016/S0140-6736(21)00370-6.

[24] L.J. Carter, L.V. Garner, J.W. Smoot, Y. Li, Q. Zhou, C.J. Saveson, J.M. Sasso, A.C. Gregg, D.J. Soares, T.R. Beskid, Assay techniques and test development for COVID-19 diagnosis, ACS Cent. Sci. 6 (2020) 591–605, doi:10.1021/acscentsci.0c00501.

[25] S. Talebian, G.G. Wallace, A. Schroeder, F. Stellacci, J. Conde, Nanotechnology-based disinfectants and sensors for SARS-CoV-2, Nat. Nanotechnol. 15 (2020) 618–621, doi:10.1038/s41565-020-0751-0.

[26] B.D. Kevadiya, J. Machhi, J. Herskovitz, M.D. Oleynikov, W.R. Blomberg, N. Bajwa, D. Soni, S. Das, M. Hasan, M. Patel, Diagnostics for SARS-CoV-2 infections, Nat. Mater. 20 (2021) 593–605, doi:10.1038/s41563-020-00906-z.

[27] M.J. Mina, K.G. Andersen, COVID-19 testing: one size does not fit all, Science 371 (2021) 126–127, doi:10.1126/science.abe9187.

[28] J. Cheong, H. Yu, C.Y. Lee, J.U. Lee, H.J. Choi, J.H. Lee, H. Lee, J. Cheon, Fast detection of SARS-CoV-2 RNA via the integration of plasmonic thermocycling and fluorescence detection in a portable device, Nat. Biomed. Eng. 4 (2020) 1159–1167, doi:10.1038/s41551-020-00654-0.

[29] B. Udugama, P. Kadhiresan, H.N. Kozlowski, A. Malekjahani, M. Osborne, V.Y. Li, H. Chen, S. Mubareka, J.B. Gubbay, W.C. Chan, Diagnosing COVID-19: the disease and tools for detection, ACS Nano 14 (2020) 3822–3835, doi:10.1021/acsnano.0c02624.

[30] J.D. Whitman, J. Hiatt, C.T. Mowery, B.R. Shy, R. Yu, T.N. Yamamoto, U. Rathore, G.M. Goldgof, C. Whitty, J.M. Woo, Evaluation of SARS-CoV-2 serology assays reveals a range of test performance, Nat. Biotechnol. 38 (2020) 1174–1183, doi:10.1038/s41587-020-0659-0.

[31] Z. Qin, R. Peng, I.K. Baravik, X. Liu, Fighting COVID-19: integrated micro-and nanosystems for viral infection diagnostics, Matter 3 (2020) 628–651, doi:10.1016/j.matt.2020.06.015.

[32] M. Alafeef, K. Dighe, P. Moitra, D. Pan, Rapid, ultrasensitive, and quantitative detection of SARS-CoV-2 using antisense oligonucleotides directed electrochemical biosensor chip, ACS Nano 14 (2020) 17028–17045, doi:10.1021/acsnano.0c06392.

[33] H. Li, L. Rothberg, Colorimetric detection of DNA sequences based on electrostatic interactions with unmodified gold nanoparticles, Proc. Natl. Acad. Sci. U.S.A. 101 (2004) 14036–14039, doi:10.1073/pnas.0406115101.

[34] Q. He, Q. Wu, X. Feng, Z. Liao, W. Peng, Y. Liu, D. Peng, Z. Liu, M. Mo, Interfacing DNA with nanoparticles: surface science and its applications in biosensing, Int. J. Biol. Macromol. 151 (2020) 757–780, doi:10.1016/j.ijbiomac.2020.02.217.

[35] N. Farkhari, S. Abbasian, A. Moshaii, M. Nikkhah, Mechanism of adsorption of single and double stranded DNA on gold and silver nanoparticles: investigating some important parameters in bio-sensing applications, Colloids Surf. B 148 (2016) 657–664, doi:10.1016/j.colsurfb.2016.09.022.

[36] A.H. Loo, A. Bonanni, A. Ambrosi, M. Pumera, Molybdenum disulfide (MoS₂) nanoflakes as inherently electroactive labels for DNA hybridization detection, Nanoscale 6 (2014) 11971–11975, doi:10.1039/C4NR03795B.

[37] C. Zhu, Z. Zeng, H. Li, F. Li, C. Fan, H. Zhang, Single-layer MoS₂-based nanoprobes for homogeneous detection of biomolecules, J. Am. Chem. Soc. 135 (2013) 5998–6001, doi:10.1021/ja4019572.

[38] J. Kim, K.S. Lee, E.B. Kim, S. Paik, C.L. Chang, T.J. Park, H.J. Kim, J. Lee, Early detection of the growth of Mycobacterium tuberculosis using magnetophoretic immunoassay in liquid culture, Biosens. Bioelectron. 96 (2017) 68–76, doi:10.1016/j.bios.2017.04.025.

[39] J. Kim, M. Jang, K.G. Lee, K.S. Lee, S.J. Lee, K.W. Ro, I.S. Kang, B.D. Jeong, T.J. Park, H.J. Kim, J. Lee, Plastic-chip-based magnetophoretic immunoassay for point-of-care diagnosis of tuberculosis, ACS Appl. Mater. Interfaces 8 (2016) 23489–23497, doi:10.1021/acsami.6b06924.

[40] V.T. Tran, H. Zhou, J.Y. Park, J. Kim, J. Lee, Silver-enhanced conductivity of magnetoplasmonic nanochains, Curr. Appl. Phys. 15 (2015) 110–114, doi:10.1016/j.cap.2014.11.013.

[41] L. Zhang, T. Petit, Y. Lu, B.E. Kratochvil, K.E. Peyer, R. Pei, J. Lou, B.J. Nelson, Controlled propulsion and cargo transport of rotating nickel nanowires near a patterned solid surface, ACS Nano 4 (2010) 6228–6234, doi:10.1021/nn101861n.

[42] P.J. Vach, P. Fratzl, S. Klumpp, D. Faivre, Fast magnetic micropropellers with random shapes, Nano Lett. 15 (2015) 7064–7070, doi:10.1021/acs.nanolett.5b03131.

[43] L.V. Sigolaeva, T.V. Bulko, A.Y. Konyakhina, A.V. Kuzikov, R.A. Masamrekh, J.B. Max, M. Köhler, F.H. Schacher, D.V. Pergushov, V.V. Shumyantseva, Rational design of amphiphilic diblock copolymer/MWCNT surface modifiers and their application for direct electrochemical sensing of DNA, Polymers 12 (2020) 1514 (Basel), doi:10.3390/polym12071514.

[44] H. Li, X. Wang, Z. Yu, Electrochemical biosensor for sensitively simultaneous determination of dopamine, uric acid, guanine, and adenine based on polymelamine and nano Ag hybridized film-modified electrode, J. Solid State Electrochem. 18 (2014) 105–113, doi:10.1007/s10008-013-2242-9.

[45] L.T. Tufa, S. Oh, J. Kim, K.J. Jeong, T.J. Park, H.J. Kim, J. Lee, Electrochemical immunosensor using nanotriplex of graphene quantum dots, Fe₃O₄, and Ag nanoparticles for tuberculosis, Electrochim. Acta 290 (2018) 369–377, doi:10.1016/j.electacta.2018.09.108.

[46] S. Shahrokhian, S. Rastgar, M. Amini, M. Adeli, Fabrication of a modified electrode based on Fe₃O₄ NPs/MWCNT nanocomposite: application to simultaneous determination of guanine and adenine in DNA, Bioelectrochemistry 86 (2012) 78–86, doi:10.1016/j.bioelechem.2012.02.004.